


# Effects of asymmetric material response on the mechanical behavior of porous shape memory alloys

*Journal of Intelligent Material Systems and Structures*  
2016, Vol. 27(12) 1687–1701  
© The Author(s) 2015  
Reprints and permissions:  
sagepub.co.uk/journalsPermissions.nav  
DOI: 10.1177/1045389X15604232  
jim.sagepub.com  


**Mohammad Reza Karamooz Ravari, Mahmoud Kadkhodaei and Abbas Ghaei**

## Abstract

The demand for lightweight devices attracts attention toward porous materials. Among them, porous shape memory alloys are of interest due to superior mechanical and biological properties. High cost related to fabrication and characterization of such materials makes it necessary to model their mechanical properties before fabrication. Experimental observations of dense shape memory alloys show tension–compression asymmetry which in turn can affect the mechanical response of porous ones. In this article, the effects of this asymmetric response on the mechanical response of porous shape memory alloys are investigated by comparing three models: asymmetric, symmetric with tensile, and symmetric with compressive material parameters. To this end, a constitutive model considering asymmetric material response is proposed based on microplane theory. Then, this model is used to simulate the stress–strain response of porous shape memory alloys. The results are compared with available experimental and numerical data, and a good agreement is observed. It is concluded that in comparison with the asymmetric model, the symmetric model with tensile material parameters under-predicts the stress level while the model with compressive one over-predicts the stress level. In addition, the effects of porosity on the asymmetric response as well as hysteresis of stress–strain curve in tension and compression are assessed.

## Keywords

tension–compression asymmetry, shape memory alloy, cellular lattice structure, porous material, finite element model, unit cell model, constitutive modeling

## Introduction

Since the fabrication of first porous shape memory alloys (PSMAs) in the 1990s, they have found several applications in biology, aerospace, and civil engineering due to their superior mechanical properties and biocompatibility (Mehrabi et al., 2015). The increasing demand for using these advanced materials have motivated the researchers worldwide to develop powerful modeling approaches to simulate their mechanical responses. In this regard, several modeling approaches such as finite element (DeGiorgi and Qidwai, 2002; Hassan et al., 2009; Michailidis et al., 2009; Panico and Brinson, 2008; Qidwai et al., 2001; Shariat et al., 2013; Zhu et al., 2013, 2014), micromechanical averaging (Entchev and Lagoudas, 2002, 2004; Freed et al., 2008; Liu et al., 2014; Nemat-Nasser et al., 2005; Olsen and Zhang, 2012; Toi and Choi, 2008; Zhao et al., 2005; Zhao and Taya, 2007; Zhu and Dui, 2011), phenomenological (Sayed et al., 2012), theoretical (Liu et al., 2012), and scaling methods (Maîtrejean et al., 2013a,

2013b) have been developed. It has been previously shown that microplane theory can be successfully used for modeling the three-dimensional (3D) behavior of shape memory alloys (SMAs). The idea of utilizing microplane theory for this purpose was first proposed by Brocca et al. (2002) and has been further developed by Kadkhodaei et al. (2007a, 2007b) and Mehrabi et al. (2013). This constitutive modeling approach has been shown to be thermodynamically consistent (Mehrabi et al., 2014c) and capable of modeling nonproportional loading paths (Kadkhodaei et al., 2007a, 2007b; Mehrabi et al., 2014c, 2014d). Mehrabi et al. (2014b) used the microplane theory to develop a constitutive

---

Department of Mechanical Engineering, Isfahan University of Technology, Isfahan, Iran

### Corresponding author:

Mohammad Reza Karamooz Ravari, Department of Mechanical Engineering, Isfahan University of Technology, Isfahan 84156-83111, Iran.  
Email: m.karamoozravari@me.iut.ac.ir

model for tension–torsion coupling and tension–compression asymmetry in NiTi SMAs. To take tension–compression asymmetry into account, they employed a modified phase diagram for uniaxial loading and chose the material parameters based on the loading direction, that is, tension or compression. Since no transformation function was used, this method could be used only for uniaxial loading and would be inapplicable for multi-axial loadings.

Finite element method has been used by several researchers to investigate the mechanical properties of PSMAs. DeGiorgi and Qidwai (2002) used a mesoscale technique based on two-dimensional (2D) finite element method to determine effective material response. They considered a PSMA as a combination of dense SMA and randomly distributed pores. Panico and Brinson (2008) studied the mesoscopic behavior of PSMAs using 3D finite element method. They modeled pores by allocating zero stiffness to some randomly chosen elements. The evolution of plastic strains as well as martensite transformation has also been studied. Zhu et al. (2013) used a 3D constitutive model to examine localization of phase transformation field due to the presence of structured arrays of holes in a NiTi plate. In another work (Zhu et al., 2014), they used a similar approach to assess interactions between transformation and plastic deformation of those plates.

In another approach, a PSMA is considered as a composite material with SMA as matrix and pores as inclusions. Then, the micromechanical averaging methods are used to obtain the macroscopic mechanical response. Using this method, Qidwai et al. (2001) estimated PSMAs' thermomechanical behavior by considering randomly distributed spherical and cylindrical pores. Entchev and Lagoudas (2002) established the effective elastic and inelastic behaviors of PSMAs based on the information about the mechanical response of the individual phases, shape, and volume fraction of pores. Zhao et al. (2005) presented a model for the macroscopic compressive behavior of superelastic PSMAs using Eshelby's inhomogeneous inclusion method. Entchev and Lagoudas (2004) used an incremental formulation of the Mori–Tanaka averaging scheme in combination with transformation-induced plasticity constitutive model for fully dense SMAs (Lagoudas and Entchev, 2004) to simulate effective mechanical behavior of PSMAs. Nemat-Nasser et al. (2005) modeled PSMAs as three-phase composite materials with austenite as the matrix and martensite and voids as the embedded inclusions. Zhao and Taya (2007) proposed two models, open cell and close cell, by considering spherical and ellipsoidal pore shapes. Toi and Choi (2008) developed an existing one-dimensional (1D) constitutive model for SMAs to account for the porosity and strain rate effects using porosity and martensite volume fraction as internal variables.

Experimental observations (Bechle and Kyriakides, 2014; Gall et al., 1999; Reedlunn et al., 2014; Thamburaja and Anand, 2001; Zhu and Dui, 2010) show that the mechanical stress–strain response of dense SMAs is asymmetric in tension and compression. This asymmetric response is because of an asymmetric transformation surface. Since a PSMA can be considered as a cluster of connecting ligaments, the asymmetric response of dense SMAs can severely affect the mechanical response of PSMAs. So far, several investigations have been performed on the development of asymmetric constitutive models for dense SMAs (Auricchio and Petrini, 2004; Auricchio and Taylor, 1997; Bouvet et al., 2004; Lagoudas et al., 2006; LExcellent et al., 2006; Lubliner and Auricchio, 1996; Paiva et al., 2005; Qidwai and Lagoudas, 2000; Saint-Sulpice et al., 2009; Sedlak et al., 2012; Yu et al., 2013). However, there is only a few studies that assess the effects of asymmetry for PSMAs (Liu et al., 2014; Zhu and Dui, 2011). Zhu and Dui (2011) proposed a micromechanical constitutive model for macroscopic behavior of porous NiTi. They considered the first invariant of stress tensor as the source of the tensile–compressive asymmetry. Liu et al. (2014) presented a yield function for PSMAs considering both the effect of hydrostatic stress and tensile–compressive asymmetry. In these two studies, only the tensile–compressive stress–strain response of PSMAs is compared, and the effects of asymmetry material response of dense SMAs on the response are not considered.

To the best of authors' knowledge, the effects of material asymmetric response of dense SMAs on the mechanical behavior of PSMAs have not been considered by previous studies. In this article, a 3D constitutive model is proposed for dense SMAs based on the microplane theory which takes the material asymmetry into account. Then, this constitutive model is used for investigation of the stress–strain response of PSMAs using finite element analysis. The results show good agreements with previously reported findings. In addition, the effects of asymmetry on the stress–strain response of PSMAs as well as SMA cellular lattices are assessed by comparing the results of symmetric and asymmetric models (AMs). The results indicate that a symmetric model with the tensile material parameters under-predicts the stress level, while that model with compressive ones over-predicts the stress level. In addition, the effects of porosity on the asymmetric stress–strain response of PSMAs in tension and compression as well as the hysteresis area are analyzed. For the case of SMA cellular lattices, the effects of material asymmetry as well as deformation mechanisms are investigated for body-centered cubic (BCC) and reinforced body-centered cubic (BCC-Z) microstructures with several values of porosity.

### Methodology

#### Constitutive modeling

The main idea of microplane theory is to generalize 1D constitutive laws to 3D ones which allows to use just the material parameters of uniaxial tension (compression) tests. To derive macroscopic governing equations, two main formulations can be employed, namely, “static constraint” and “kinematic constraint.” In the former formulation, the stress vector on each microplane is supposed to be the projection of macroscopic stress tensor, while in the latter, this projection rule is considered for strain vector and macroscopic strain tensor. In fact, ordinary constitutive modeling approaches, where both constraints co-exist, utilize the so-called double-constraint formulation in this regard. Carol and Bazant (1997) showed that using the kinematic constraint formulation, the obtained constitutive relations could be just used for a limited range of Poisson’s ratio. Accordingly, in this article, the static constraint formulation is utilized for the evolution of SMA constitutive relations. In this formulation, three main steps should be followed: first, the projection of stress tensor is found on each microplane as normal and shear stress vectors; then, a 1D constitutive relation is defined for each normal and shear component, and finally a homogenization process is utilized to generalize the 1D model to 3D one (Kadkhodaei et al., 2007a, 2007b; Mehrabi et al., 2014a, 2014b, 2014c, 2014d; Mehrabi and Kadkhodaei, 2013). Figure 1 shows the projected stress tensor on a generic microplane as shear and normal components. Considering  $n_i$  as the components of the unit normal vector ( $\mathbf{n}$ ) to a microplane, the traction vector on a microplane ( $t_i$ ) can be written as follows

$$t_i = \sigma_{ij}n_j \tag{1}$$

in which  $\sigma_{ij}$  is the macroscopic stress tensor. The normal stress on a microplane,  $\sigma_N$ , is formulated as the scalar projection of traction vector onto unit normal vector as

$$\sigma_N = \sigma_{ij}n_i n_j = \sigma_{ij}N_{ij} \tag{2}$$

Referring to Figure 1, the shear component of the traction vector is obtained as the subtraction of normal stress vector from traction vector which yields

$$\sigma_{Ti} = t_i - \sigma_N n_i \tag{3}$$

The magnitude of the shear stress on a microplane is calculated as

$$\sigma_T = \sigma_{Ti} \sigma_{Ti} \tag{4}$$

By substituting equation (3) into equation (4) and some algebraic simplifications, the magnitude of the shear stress component can be expressed as follows

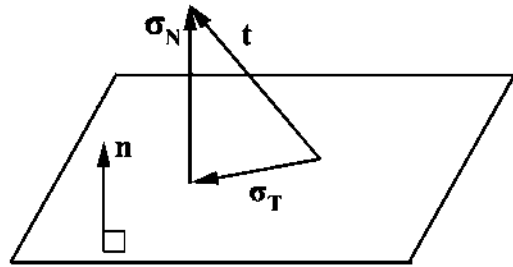


Figure 1. Projection of stress tensor as normal and shear stress vectors on each microplane.

$$\sigma_T = T_{ij} \sigma_{ij} \tag{5}$$

where  $T_{ij} = (\hat{t}_i n_j + \hat{t}_j n_i)/2$  in which  $\hat{t}_i = (\sigma_{ik} n_k - \sigma_N n_i) / \sqrt{\sigma_{jr} \sigma_{js} n_r n_s - \sigma_N^2}$  is the unit vector parallel to resultant shear stress on the plane. It has been previously shown that using the static constraint formulation with volumetric–deviatoric split, that is,  $\sigma_N = \sigma_V + \sigma_D$ , the elastic part of a microplane constitutive equation exhibits double constraint (Kadkhodaei et al., 2007a; Mehrabi and Kadkhodaei, 2013), and the microlevel elastic moduli are equal to the macroscopic ones (Kadkhodaei et al., 2007a). It is also supposed that the martensite transformation is just associated with the shear component of microplane stresses (Kadkhodaei et al., 2007a, 2007b). Based on this assumption, the volumetric and deviatoric parts of the normal component of the strain vector can be related to the corresponding stresses using Hook’s law, and the shear strain is calculated using the 1D relation proposed for SMAs by Poorasadion et al. (2013)

$$\varepsilon_V = \frac{1 - 2\nu}{E} \sigma_V \tag{6}$$

$$\varepsilon_D = \frac{1 + \nu}{E} \sigma_D \tag{7}$$

$$\varepsilon_T = \frac{1 + \nu}{E} \sigma_T + \varepsilon_L^+ \xi_s^+ + \varepsilon_L^- \xi_s^- \tag{8}$$

in the relationships above,  $\nu$  is SMA’s Poisson’s ratio;  $\varepsilon_V$  is the volumetric strain;  $\varepsilon_D$  is the deviatoric strain;  $\varepsilon_T$  is the shear strain;  $\varepsilon_L^+$  and  $\varepsilon_L^-$  are the maximum recoverable strains in uniaxial tension and compression, respectively; and  $E$  is the macroscopic elastic modulus which can be described as a function of martensite volume fraction (Poorasadion et al., 2013)

$$\frac{1}{E} = \frac{1}{E_A} + \xi_s^+ \left( \frac{1}{E_M^+} - \frac{1}{E_A} \right) + \xi_s^- \left( \frac{1}{E_M^-} - \frac{1}{E_A} \right) + \xi_T \left( \frac{1}{E_M^T} - \frac{1}{E_A} \right) \tag{9}$$

where  $E_A$  is fully austenite elastic modulus;  $E_M$  is fully martensite elastic modulus; and  $\xi_s$  and  $\xi_T$  are stress-

and temperature-induced martensite volume fractions, respectively. The superscripts “+” and “-” denote tension and compression, correspondingly. The superscript “*T*” is attributed to temperature-induced quantities. In this article, two internal variables related to martensite volume fraction are considered to be able to distinguish between tension and compression. In addition, equation (9) indicates that the effects of different martensite elastic moduli in tension and compression are taken into account.

To generalize the 1D constitutive relations to 3D ones, the principle of complementary virtual work is utilized which yields (Kadkhodaei et al., 2007a, 2007b)

$$\frac{4\pi}{3} \varepsilon_{ij} \sigma_{ij} = 2 \int_{\Omega} (\varepsilon_V \delta \sigma_V + \varepsilon_D \delta \sigma_D + \varepsilon_T \delta \sigma_T) d\Omega \quad (10)$$

where  $\Omega$  is the surface of a unit hemisphere and  $\varepsilon_{ij}$  is the macroscopic strain tensor. By substituting equations (2) and (6) to (8) into equation (10) and taking the independence of individual components of virtual stress tensor into account, the following equation is obtained

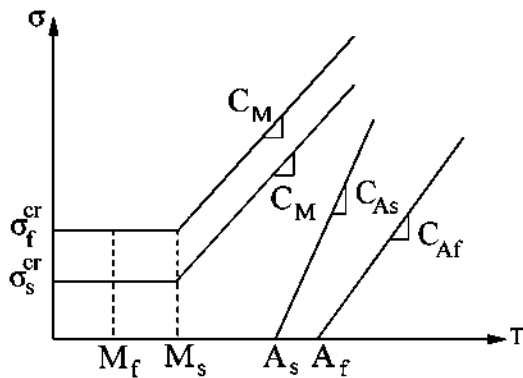


Figure 2. Employed phase diagram for shape memory alloys.

$$\varepsilon_{ij} = -\frac{\nu}{E} \sigma_{mm} \delta_{ij} + \frac{1+\nu}{E} \sigma_{mn} \cdot \frac{3}{2\pi} \int_{\Omega} (N_{mn} N_{ij} + T_{mn} T_{ij}) d\Omega + (\varepsilon_L^+ \xi_s^+ + \varepsilon_L^- \xi_s^-) \cdot \frac{3}{2\pi} \int_{\Omega} T_{ij} d\Omega \quad (11)$$

It is also necessary to explain the evolution of martensite volume fraction during transformation in tension and compression. In this regard, as shown in Figure 2, the proposed phase diagram by Sameallah et al. (2014) is utilized. In this diagram,  $M_f$ ,  $M_s$ ,  $A_s$ , and  $A_f$  are martensite finish, martensite start, austenite start, and austenite finish temperatures, respectively.  $\sigma_s^{cr}$  and  $\sigma_f^{cr}$  are the critical start and finish stresses for martensite detwinning, respectively, and  $C_M$ ,  $C_{A_s}$ , and  $C_{A_f}$  are the slopes of stress–temperature diagram.

When temperature is below  $M_s$ , by applying stress, twinned martensite starts to transform to detwinned one when the stress reaches the critical value  $\sigma_s^{cr}$ . The detwinning process will be completed by the value of stress  $\sigma_f^{cr}$ . For temperatures higher than  $M_s$ , the transformation of austenite to martensite starts when the applied stress is equal to  $\sigma_s^{cr} + C_M(T - M_s)$ , and this transformation finishes at the stress of  $\sigma_f^{cr} + C_M(T - M_s)$ . Similarly, for temperatures higher than  $A_s$ , transformation from martensite to austenite starts at the stress of  $C_{A_s}(T - A_s)$  and finishes at  $C_{A_f}(T - A_f)$ .

One must use this phase diagram with precaution for high temperatures. At high temperatures, the lines related to the austenite band may cross those of the martensite band. As shown in Figure 3, this issue would be problematic when the critical stress of austenite finish is higher than that of martensite start or if the critical stress of austenite start is higher than that of martensite finish. It means that this phase diagram should be used by implying the following constraints

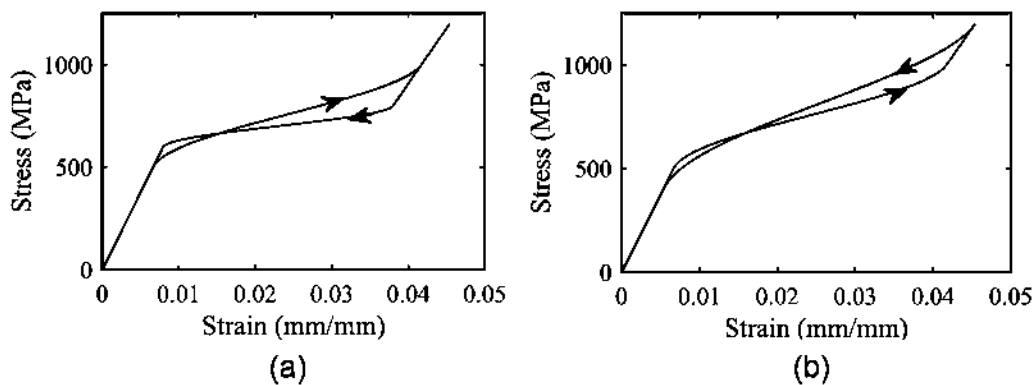


Figure 3. Stress–strain curve of an SMA when (a) the critical stress of austenite finish is higher than that of martensite start and (b) the critical stress of austenite start is higher than that of martensite finish.

$$C_{As}(T - A_s) < \sigma_{cr}^f + C_M(T - M_s) \quad (12)$$

$$C_{Af}(T - A_f) < \sigma_{cr}^s + C_M(T - M_s) \quad (13)$$

Using the above two equations and considering  $M_d$  as the martensite dead temperature, the maximum value of the temperature can be calculated as

$$T_{max} = \min\left(\frac{(C_{Af}A_f + \sigma_{cr}^s - C_M M_s)}{C_{Af} - C_M}, \frac{(C_{As}A_s + \sigma_{cr}^f - C_M M_s)}{C_{As} - C_M}, M_d\right) \quad (14)$$

To evaluate the value of martensite volume fractions in tension and compression, in this article, the evolution function of martensite volume fraction presented by Poorasadion et al. (2013) is modified based on this phase diagram as follows

$$\left\{ \begin{array}{l} \text{if } T \leq M_s \text{ and } \sigma_s^{cr} < \hat{\sigma} < \sigma_f^{cr} : \\ Y = \cos\left(\frac{\pi}{\sigma_f^{cr} - \sigma_s^{cr}}(\hat{\sigma} - \sigma_s^{cr})\right) \\ \xi_s^r = \frac{1-Y}{2} + \xi_{s0}^r \frac{1+Y}{2}, \xi_s^p = \xi_{s0}^p \frac{1-\xi_s^r}{1-\xi_{s0}^r}, \xi_T = (\xi_{T0} + \Delta) \frac{1-\xi_s^r}{1-\xi_{s0}^r} \\ \text{if } T < M_f : \Delta = 0 \\ \text{else} : \Delta = \frac{1-\xi_0}{2}(1 - Y_{MT}) \\ \text{if } T > M_s \text{ and } \sigma_s^{cr} + C_M(T - M_s) < \hat{\sigma} < \sigma_f^{cr} + C_M(T - M_s) : \\ Y = \cos\left(\frac{\pi}{\sigma_f^{cr} - \sigma_s^{cr}}(\hat{\sigma} - \sigma_s^{cr} - C_M(T - M_s))\right) \\ \xi_s^r = \frac{1-Y}{2} + \xi_{s0}^r \frac{1+Y}{2}, \xi_s^p = \xi_{s0}^p \frac{1-\xi_s^r}{1-\xi_{s0}^r}, \xi_T = \xi_{T0} \frac{1-\xi_s^r}{1-\xi_{s0}^r} \\ \text{if } T > A_s \text{ and } C_{Af}(T - A_f) < \hat{\sigma} < C_{As}(T - A_s) : \\ Y = \cos\left(\frac{\pi}{C_{As}(T - A_s) - C_{Af}(T - A_f)}(C_{As}(T - A_s) - \hat{\sigma})\right) \\ \xi_s^r = \frac{\xi_{s0}^r}{2}(1 + Y), \xi_s^p = \frac{\xi_{s0}^p}{2}(1 + Y), \xi_T = \frac{\xi_{T0}}{2}(1 + Y) \\ \text{if } M_f < T < M_s \text{ and } \hat{\sigma} < \sigma_s^{cr} \\ \xi_s^r = \xi_{s0}^r, \xi_s^p = \xi_{s0}^p, \xi_T = \frac{1-\xi_0}{2}(1 - Y_{MT}) + \xi_{T0} \end{array} \right. \quad (15)$$

in which superscripts “r” and “p” are as ( $r = +$ ,  $p = -$ ) in tension and ( $r = -$ ,  $p = +$ ) in compression;  $\xi_{s0}^r$ ,  $\xi_{s0}^p$ , and  $\xi_{T0}$  are the initial values of the corresponding martensite volume fraction;  $Y_{MT} = \cos(\pi(T - M_s)/(M_f - M_s))$ ; and  $\hat{\sigma}$  is the modified equivalent stress to account for asymmetric material response as follows

$$\hat{\sigma} = \frac{1}{1 + \beta} \left\{ \sqrt{3}J_2 + \frac{9}{2}\beta \frac{J_3}{J_2} \right\} \quad (16)$$

in which  $\beta$  is a parameter to determine the value of asymmetry, and  $J_2$  and  $J_3$  are the second and third invariants of deviatoric stress tensor, respectively. For  $\beta = 0$ , the equivalent stress,  $\hat{\sigma}$ , is reduced to von-Mises equivalent stress, and the constitutive model will be symmetric. According to experimental observations, the transformation surfaces of martensite to austenite and austenite to martensite might be of different levels

of asymmetry which could be taken into account using different values of  $\beta$  presented by

$$\beta = \begin{cases} \beta_1 & \text{if } \dot{\sigma} > 0 \\ \beta_2 & \text{if } \dot{\sigma} < 0 \end{cases} \quad (17)$$

The parameters  $\beta_1$  and  $\beta_2$  are chosen to distinguish the asymmetry level in loading from unloading. Finally, using equations (9), (11), (15), and (16) under the limitations of equation (14), one can model the 3D constitutive response of SMAs.

### Unit cell models for porous materials

In this section, three cases including 13% porous NiTi, 42% porous NiTi, and BCC as well as BCC-Z SMA cellular lattice structures with the porosities of 25.2%, 44.30%, 64.25%, and 82.15% are used to assess the effects of asymmetric response of dense SMA on the mechanical response of porous specimens in tension and compression. For each case, a repeating unit cell representing the microstructure of porous sample is used in combination with suitable boundary conditions. In the rest of this section, first, the repeating unit cell models are explained and then the applied boundary conditions are introduced.

**Case 1: 13% porous NiTi.** Figure 4(a) shows the microstructure of 13% porous NiTi fabricated by Zhao et al. (2005). Referring to this figure, the microstructure may be represented as the intersection of some spheres. Since the sample is fabricated by spark plasma sintering, these spheres are the powder particles sintered with each other. Based on this observation, the unit cell shown in Figure 4(b) is used for modeling purposes. This unit cell is constructed by putting eight spheres with the radius of “R” on the corners of a cube with the length of  $L = 2 \times (1 - \delta) \times R$  meaning that two spheres are penetrated to each other with a value of  $2 \times \delta \times R$ . The amount of porosity can be adjusted by changing the value of  $\delta$  as shown in Figure 5. Based on this figure, to achieve the value of 13% for porosity,  $\delta = 0.21265$  should be utilized.

**Case 2: 42% porous NiTi.** This subsection is allotted to the modeling of 42% porous NiTi produced by Entchev and Lagoudas (2002). Figure 6(a) shows the microstructure of 42% porous NiTi, and Figure 6(b) shows the corresponding unit cell model utilized for modeling. This unit cell is composed of a spherical pore with the radius R at the center of a cube with the length of L. In this article,  $L = 1$  is assumed, and the value of R is adjusted to satisfy the desirable amount of porosity. Figure 7 shows the value of porosity as a function of pore’s radius. Using this curve,  $R = 0.4646$  should be used to obtain 42% porosity.

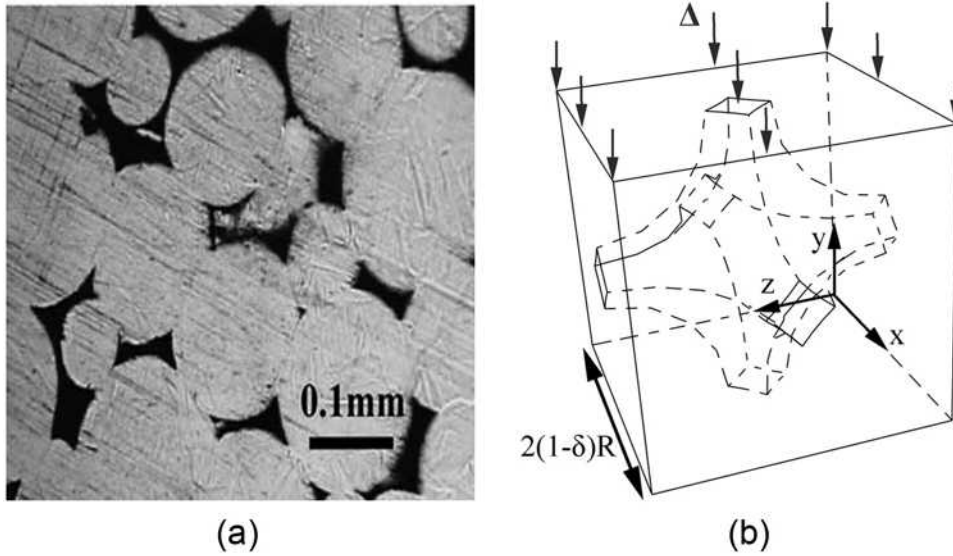


Figure 4. (a) Microstructure of 13% porous NiTi (Zhao et al., 2005) and (b) repeating unit cell model.

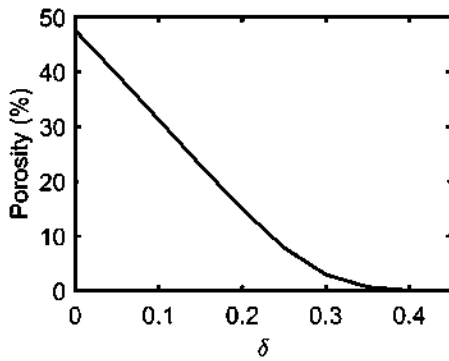


Figure 5. Variation of the porosity with the parameter  $\delta$  for case I unit cell model.

*Case 3: SMA cellular lattice structures.* Cellular lattice structures are a class of porous materials with regular microstructure which allows a designer to adjust the mechanical properties more easily than conventional porous materials. Thanks to additive manufacturing, several attempts have been made to fabricate and characterize SMA cellular lattices (Rahmanian et al., 2014). In this article, BCC and BCC-Z cellular lattice structures are used to investigate the effects of material asymmetry on the mechanical behavior of porous samples. There are two reasons for choosing these microstructures in this study: (1) it has been previously proved that these two microstructures are nearly optimized for carrying combination of loads (Karamooz Ravari et al., 2014; Karamooz Ravari and Kadkhodaei,

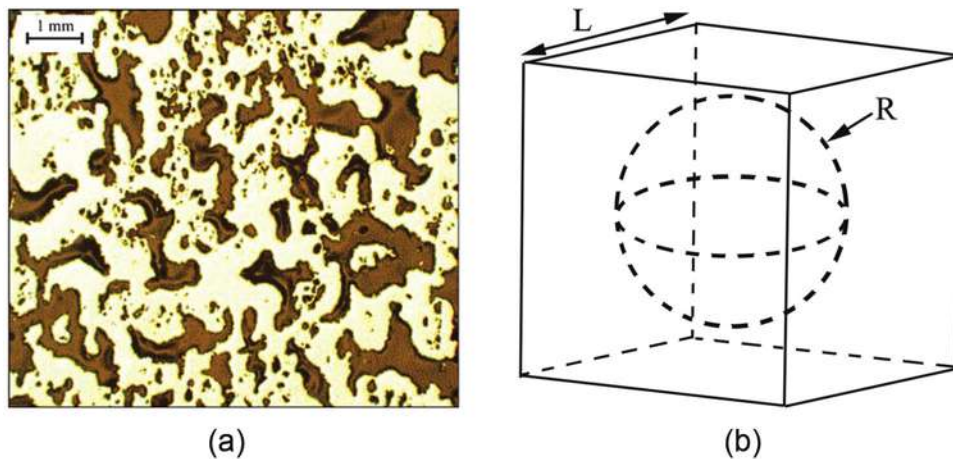
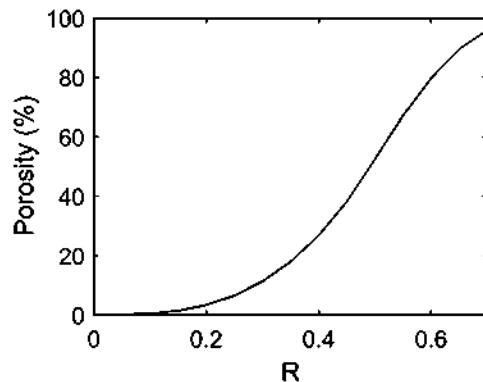


Figure 6. (a) Microstructure of 42% porous NiTi (Entchev and Lagoudas, 2002) and (b) unit cell utilized for the modeling of 42% porous NiTi.

2015), and (2) since all the struts of BCC lattice are diagonal, the main deformation mechanism is bending of the struts. Therefore, fibers of each strut experience tensile and compressive loads at the same time. For BCC-Z cellular lattice, there is one vertical strut which causes the main deformation mechanism to tend toward axial one (Karamooz Ravari and Kadkhodaei, 2013). Therefore, using these two, it is possible to assess the effects of deformation mechanisms on the asymmetric material response of porous SMAs.

Figure 8(a) and (b) shows the repeating unit cell of BCC and BCC-Z cellular lattices together with their geometrical parameters, respectively. In this figure, the cell size and struts' diameter are denoted by  $L$  and  $D$ , respectively. The amount of porosity can be adjusted by changing the value of these two geometrical parameters. In this article,  $L = 1$  is considered, and the value of  $D$  is varied to achieve the desired porosity. Figure 9 shows the variation of porosity as a function of struts' diameter for BCC and BCC-Z cellular lattice structures. Based on this curve, for the porosity values of 82.15%, 64.25%, 44.30%, and 25.20%, the value of struts' diameter is obtained to be 0.1, 0.2, 0.3, and 0.4,



**Figure 7.** Variation of the porosity with the parameter  $R$  for case 2 unit cell model.

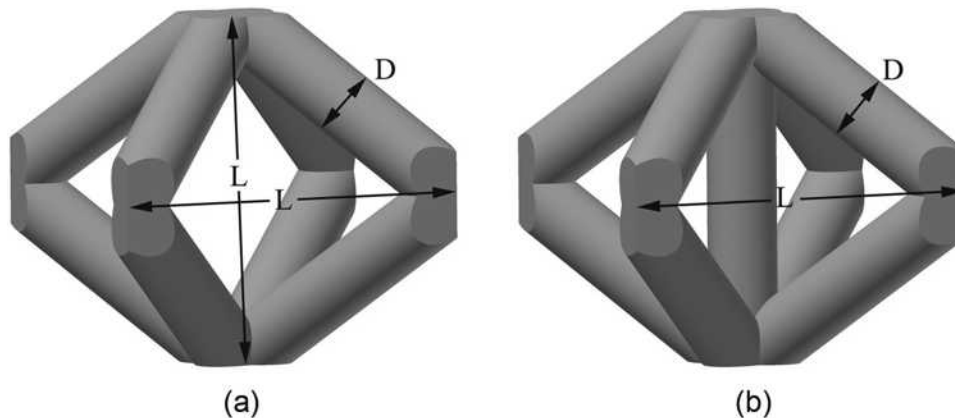


**Figure 8.** Unit cell of (a) BCC and (b) BCC-Z cellular lattice structures.

respectively, for BCC cellular lattice structure. The struts' diameters are 0.187, 0.283, 0.378, and 0.476 for BCC-Z cellular lattices.

### Periodic boundary conditions

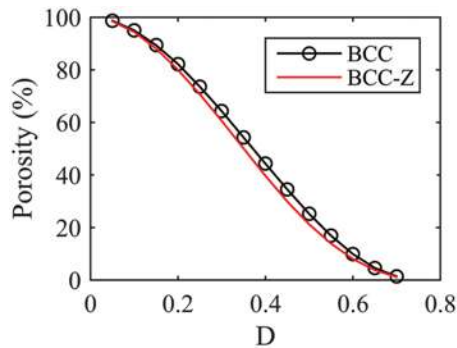
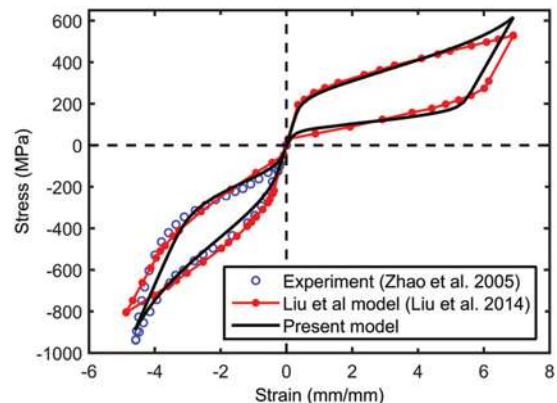
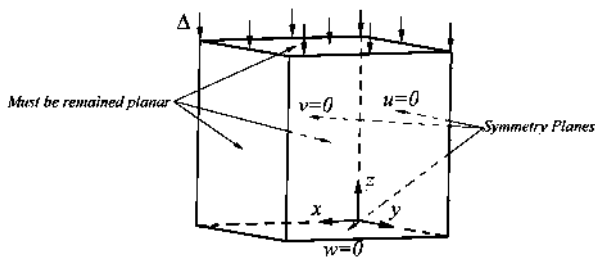
Since only one unit cell is utilized for modeling purposes, appropriate periodic boundary conditions must be imposed to the models. As all the above-mentioned unit cell models have three symmetric planes, combination of periodic and symmetric boundary conditions can be used to reduce the computational cost of the simulations. To do so, as shown in Figure 10, the translational degree of freedom normal to symmetry planes should be fixed. Beside this boundary condition, the opposite faces to symmetry ones should be forced to remain planar during the loading cycle. After imposing these boundary conditions, the upper face of the unit cell is compressed by the displacement of  $\Delta$ . More information about these boundary conditions is given by Altenbach and Oechsner (2011), Böhm (2004), and Li (2008).

### Results and discussion

In this section, first, the stress–strain response of 13% porous SMA in tension and compression is compared with previously reported experimental and numerical findings. Then, the results of other unit cell models are presented. To investigate the effects of material asymmetry in cases 2 and 3, three constitutive laws are compared including symmetric model using tensile material parameters (SMT), symmetric model using compressive material parameters (SMC), and AM. In each case, first, the utilized material parameters are introduced. For all the cases, the simulations are performed at a constant temperature and there is not any temperature-induced martensite. Therefore, for all the cases, the value of  $E_M^T$  is optional and is not presented.

**Table 1.** Material parameters utilized for 13% porous NiTi fabricated by Zhao.

$E_A$ (MPa)	$E_M^+$ (MPa)	$E_M^-$ (MPa)	$\nu$	$M_f$ ( $^{\circ}\text{C}$ )	$M_s$ ( $^{\circ}\text{C}$ )	$A_s$ ( $^{\circ}\text{C}$ )	$A_f$ ( $^{\circ}\text{C}$ )	$\sigma_s^{cr}$ (MPa)
75,000	31,000	52,000	0.33	5.39	20.65	19.3	38.82	50
$\sigma_f^{cr}$ (MPa)	$C_M$ (MPa/ $^{\circ}\text{C}$ )	$C_{As}$ (MPa/ $^{\circ}\text{C}$ )	$C_{Af}$ (MPa/ $^{\circ}\text{C}$ )	$\varepsilon_L^+$	$\varepsilon_L^-$	$\beta_1$	$\beta_2$	$T$ ( $^{\circ}\text{C}$ )
800	4.02	11.4	3.65	0.052	-0.023	0.175	0.48	58

**Figure 9.** Variation of porosity as a function of struts' diameter for BCC and BCC-Z cellular lattice structures.**Figure 11.** Stress–strain response of 13% porous SMA in tension and compression: experiment, Liu et al. (2014) model, and present model.**Figure 10.** Combination of periodic and symmetric boundary conditions.

### Case 1: 13% porous NiTi

To be able to compare the results with the previously reported ones, the material parameters presented in Table 1 are obtained based on the findings reported by Liu et al. (2014). In this regard, the material parameters are adjusted in such a way to achieve the start and finish transformation stresses which were considered as the material parameters in Liu et al. (2014). Then, the model is meshed using 10-node modified quadratic tetrahedron elements denoted by C3D10M in ABAQUS. A mesh sensitivity study is conducted by repeatedly refining the mesh size and rerunning the analysis until changes in the results are negligible. Consequently, the appropriate mesh size was found to be about  $0.2 \times R$  which forms 373 elements through the unit cell model.

Figure 11 compares the predicted stress–strain curve for 13% porous NiTi with available experimental response in compression (Zhao et al., 2005) and with the theoretical results presented by Liu et al. (2014) in

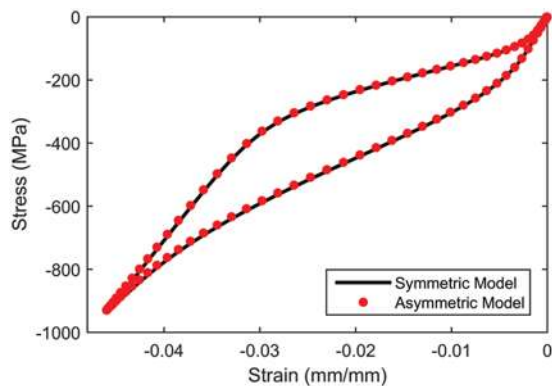
tension and compression. As shown in this figure, a good agreement is achieved between the proposed model and the experiment in compression. The results of the present model correlate very well with those reported by Liu et al. (2014) model except for strains larger than 5.6%. The discrepancy at larger strains might be due to the different transformation functions utilized in these two models. As it is seen in this figure, the initial unloading slope of tensile stress–strain curve for both models is similar; however, the value of maximum stress corresponding to the maximum applied strain is higher for the present model compared to that reported by Liu et al. (2014). The latter can also be observed in the compressive stress–strain response which shows that the Liu et al. model under-predicts the stress level. However, the transformation rate is predicted more accurately by the proposed model. In addition, at the beginning of unloading curve in compression, the proposed model predicts a smaller slope compared to the experimental response. However, this prediction is more accurate than that predicted by Liu et al. (2014). It is worth mentioning that there are no experimental results for simultaneous tensile and compressive loadings of porous SMAs. Consequently, the validity of the results still needs to be investigated in the future.

Figure 12 compares the stress–strain response of 13% porous NiTi using the symmetric model and AM. Note that the symmetric model is attributed by setting  $\beta = 0$ . It is obvious that the difference between these



**Table 2.** Material parameters attributed to case 2.

$E_A$ (MPa)	$E_M^+$ (MPa)	$E_M^-$ (MPa)	$\nu$	$M_f$ ( $^{\circ}\text{C}$ )	$M_s$ ( $^{\circ}\text{C}$ )	$A_s$ ( $^{\circ}\text{C}$ )	$A_f$ ( $^{\circ}\text{C}$ )	$\sigma_s^{cr}$ (MPa)
40,000	20,000	28,000	0.33	0.0	20.0	30.0	60.0	0.0
$\sigma_f^{cr}$ (MPa)	$C_M$ (MPa/ $^{\circ}\text{C}$ )	$C_{As}$ (MPa/ $^{\circ}\text{C}$ )	$C_{Af}$ (MPa/ $^{\circ}\text{C}$ )	$\varepsilon_L^+$	$\varepsilon_L^-$	$\beta_1$	$\beta_2$	$T$ ( $^{\circ}\text{C}$ )
0.0	7.0	7.0	7.0	0.03	-0.016	0.16	0.16	60

**Figure 12.** Comparison of stress–strain response of 13% porous NiTi obtained using symmetric and asymmetric models.

stress–strain responses is negligible, meaning that the asymmetric material response of dense SMA has a slight effect on the mechanical response of this unit cell model.

### Case 2: 42% porous NiTi

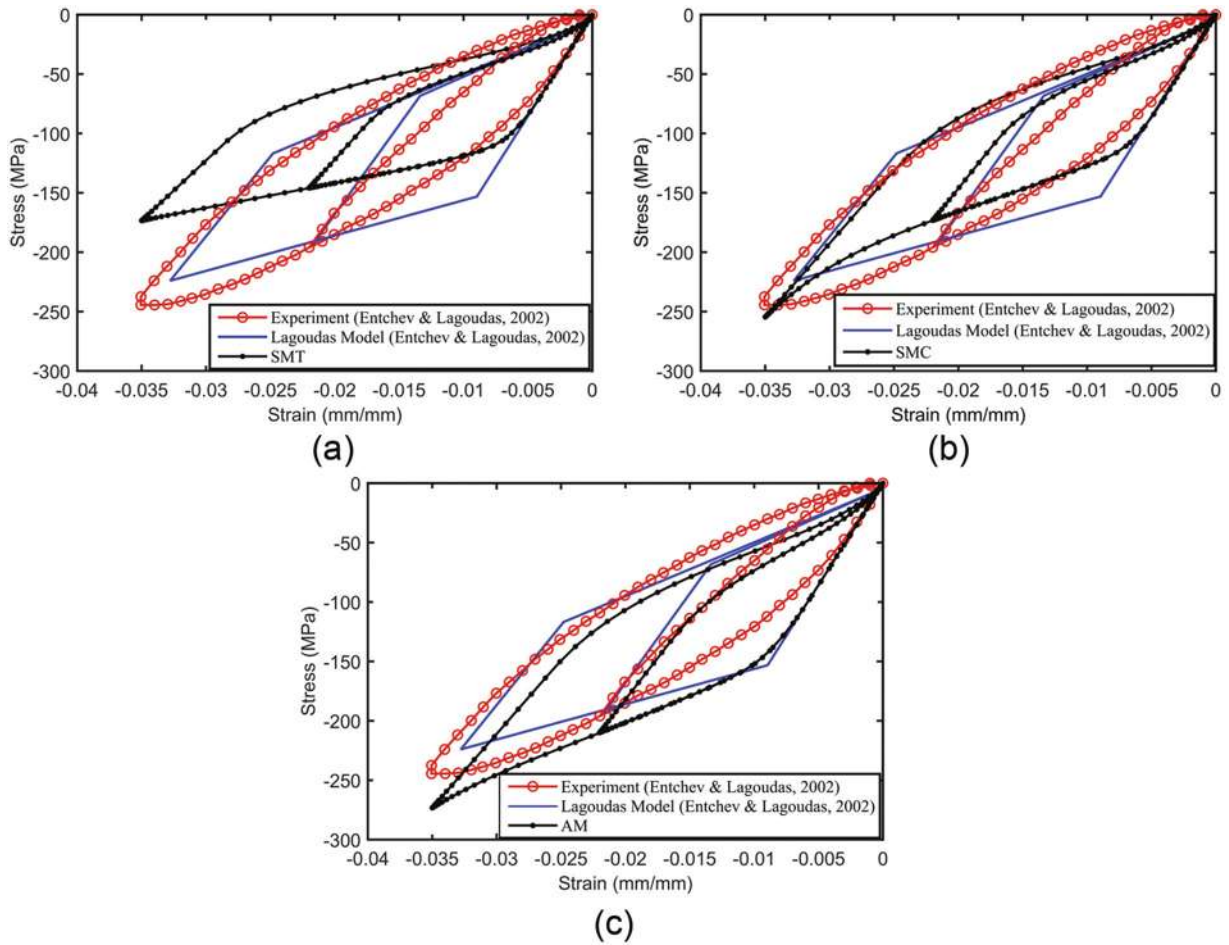
The unit cell model related to the 42% porous NiTi sample is meshed using 10-node general-purpose tetrahedron elements with improved surface stress formulation denoted by C3D10I in ABAQUS. By applying the mesh sensitivity analysis, a mesh size of about  $0.1 \times R$  is chosen for this case. The material parameters used by Entchev and Lagoudas (2002) are supposed to be related to compressive response of dense SMA. Accordingly, the material parameters corresponding to tension and asymmetric response including  $E_M^+$ ,  $\varepsilon_L^+$ ,  $\beta_1$ , and  $\beta_2$  are considered according to the experimental observations for NiTi alloys. It is observed for polycrystalline SMAs that martensite elastic moduli in compression are greater than those in tension. Also, the maximum recoverable strain in tension is about twice the compressive one. Accordingly,  $E_M^+$  is supposed to be smaller than  $E_M^-$ , and  $\varepsilon_L^+$  is taken to be about twice  $\varepsilon_L^-$  (Poorasadion et al., 2013). Moreover, it is reported that the value of asymmetric parameter ( $\beta$ ) is about 0.16 for polycrystalline NiTi (Auricchio and Taylor, 1997; Lubliner and Auricchio, 1996). Based on these facts, the material parameters presented in Table 2 are used for modeling purposes.

Figure 13(a) to (c) compares two cycles of loading–unloading stress–strain response of 42% porous NiTi

obtained by experiment and predicted by Entchev and Lagoudas (2002) model with SMT, SMC, and AM. As it is seen, the prediction of AM is more reasonable than SMT and SMC, especially for the first cycle. As a result, unlike the studied 13% porous NiTi, the asymmetric response of dense SMA has a considerable effect on the stress–strain response of 42% porous specimen. Since stress state in porous materials, especially near their pore walls, is too complicated, asymmetric material response of dense SMAs should be considered using a suitable equivalent stress rather than separate material parameters in tension and compression similar to the approach proposed by Mehrabi et al. (2014b) and Poorasadion et al. (2013).

Referring to Figure 13, it is not possible to distinguish the initiation and finish of transformations in the experimental stress–strain curves. It might be due to stress concentration in pores, especially their sharp points, which cause local transformation and smooth change in the slope of the curve (Panico and Brinson, 2008). As it is obvious, compared to the approach proposed by Entchev and Lagoudas (2002), the present model is capable of capturing this phenomenon. However, since it is supposed that the pores are spherical voids without sharp edges which are repeated uniformly through the PSMA, the effects of stress concentration is not so severe in the present work. This issue causes the predicted stress–strain response not to be as smooth as the experimental one.

Figure 14 shows the stress–strain response of 42% porous NiTi in tension and compression using the AM. It is seen that for a specific value of strain, the compressive hysteresis is bigger than the tensile one. To assess this issue more comprehensively, the stress–strain responses of the PSMA with different values of porosity are depicted in Figure 15. Note that since the solid finite element model is used, a vast range of porosity can be modeled. In this article, the value of porosity between 10% and 85% is considered for studying the effects of porosity. Figure 15 shows that an increase in the value of porosity leads to a decrease in the hysteresis of the stress–strain curve as well as the required stress for the same value of strain in both tension and compression. In addition, the difference between the hysteresis area in tension and compression decreases with the increase in the value of porosity. To prove this claim, a dimensionless parameter  $\Lambda = (A_{hist}^C - A_{hist}^T)/A_{hist}^C$  is introduced, in which  $A_{hist}^C$  and  $A_{hist}^T$  are the hysteresis areas of



**Figure 13.** Comparison of two loading–unloading cycles obtained in experiment and by Entchev and Lagoudas (2002) model with (a) SMT, (b) SMC, and (c) AM.

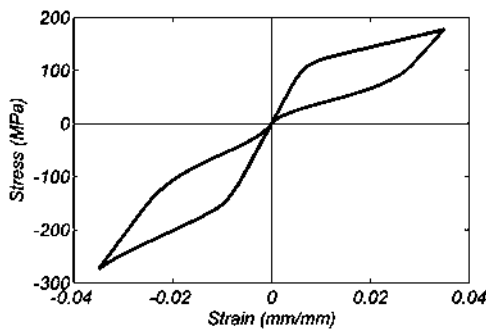


**Figure 14.** Stress–strain response of 42% porous NiTi in tension and compression obtained using the AM.

stress–strain curve in tension and compression, respectively. Variations of the parameter  $\Lambda$  with the value of porosity related to Figure 15 are shown in Figure 16. It can be concluded from this figure that the hysteresis area of stress–strain curve in tension tends to that in compression by increasing the value of porosity. The value of parameter  $\Lambda$  is about 10% for 10% porosity, while it is smaller than 0.5% for 85% porosity.

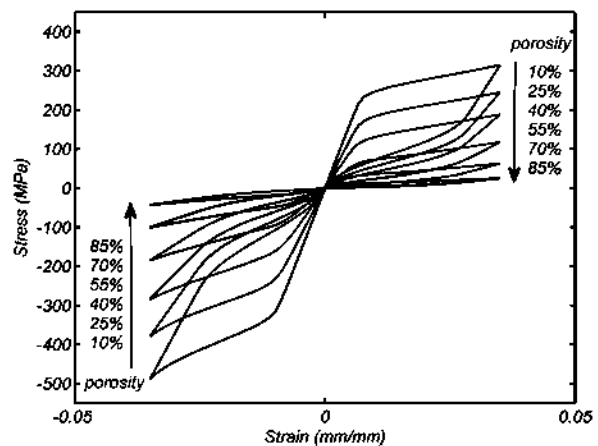


**Figure 15.** Influence of porosity on the asymmetric stress–strain response of PSMA.

**Case 3: SMA cellular lattice structures**

The model is meshed similar to case 1, and the appropriate mesh size was found to be about  $0.05 \times D$ .

**Table 3.** Material parameters utilized for case 3.

$E_A$ (MPa)	$E_M^+$ (MPa)	$E_M^-$ (MPa)	$\nu$	$M_f$ ( $^{\circ}\text{C}$ )	$M_s$ ( $^{\circ}\text{C}$ )	$A_s$ ( $^{\circ}\text{C}$ )	$A_f$ ( $^{\circ}\text{C}$ )	$\sigma_s^{cr}$ (MPa)
45,000	35,000	60,000	0.33	-40	-20	10	35	200
$\sigma_f^{cr}$ (MPa)	$C_M$ (MPa/ $^{\circ}\text{C}$ )	$C_{As}$ (MPa/ $^{\circ}\text{C}$ )	$C_{Af}$ (MPa/ $^{\circ}\text{C}$ )	$\varepsilon_L^+$	$\varepsilon_L^-$	$\beta_1$	$\beta_2$	$T$ ( $^{\circ}\text{C}$ )
500	3.75	12	12	0.045	-0.016	0.3	0.18	60

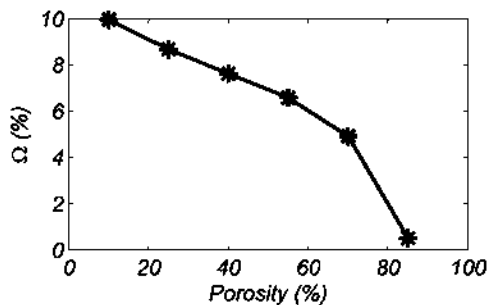
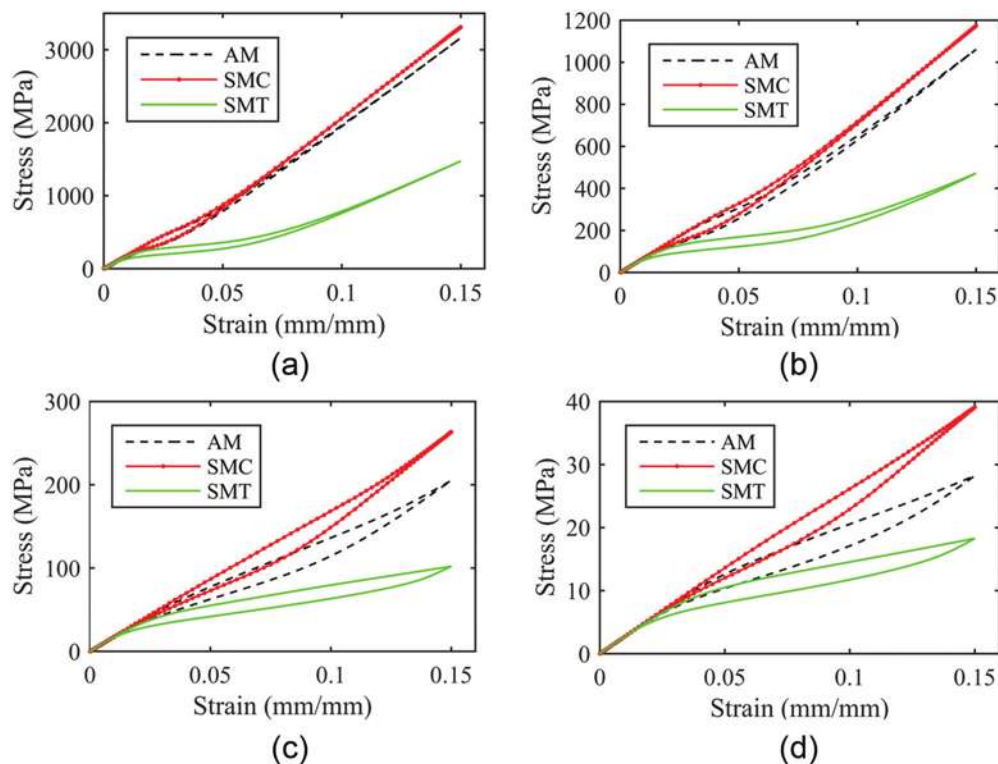
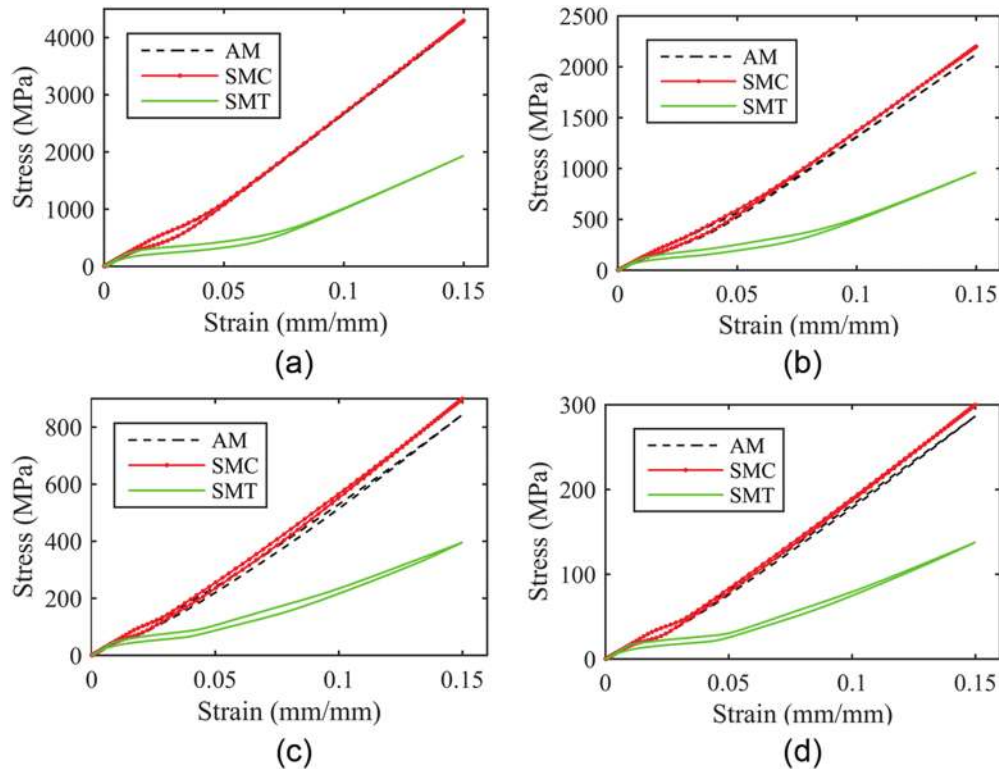
**Figure 16.** Variations of the parameter  $\Lambda$  with porosity.

Table 3 shows the material parameters utilized for these investigations.

Figure 17(a) to (d) shows the stress–strain response of BCC lattice structure using SMC, SMT, and AM for different values of porosity. It is seen that the SMC predicts stress levels higher than those by the other two

models. It might be because of higher values of stress level related to compressive stress–strain response of dense SMAs as observed in experiments. Since some fibers of each strut in the lattice experience tension while some experience compression, using the AM, the required stress at a specific strain is higher than that by SMT while it is lower than that by SMC. Moreover, the stress level in AM is closer to SMC than that in SMT. This issue can be explained such that the unit cell is supposed to carry compressive loads. Therefore, each strut is under bending as well as compression. Additionally, more fibers experience compressive loads, and the neutral axis moves toward the tensile portion. Accordingly, the stress–strain response of AM is closer to that of SMC. As another result, by decreasing the amount of porosity, the stress–strain response of AM tends to one obtained using the SMC. It is due to the fact that by increasing the value of porosity, bending in the lattice struts is more pronounced in comparison with axial

**Figure 17.** Stress–strain response of SMA with BCC cellular lattice structure with the porosity of (a) 25.20%, (b) 44.30%, (c) 64.25%, and (d) 82.15%.



**Figure 18.** Stress–strain response of SMA with BCC-Z cellular lattice structures with the porosity of (a) 25.20%, (b) 44.30%, (c) 64.25%, and (d) 82.15%.

loading, meaning that more portions of the struts experience tension.

Figure 18 compares the stress–strain response of BCC-Z cellular lattice structures obtained using SMT, SMC, and AM for different values of porosity. As it can be seen, even for high amounts of porosity, the material asymmetric response of dense SMA has a slight effect on the mechanical response of BCC-Z cellular lattices in comparison with BCC lattices. It means that the main deformation mechanism in BCC-Z lattice structure is axial contraction due to the existence of vertical strut. In addition, similar to BCC structure, by decreasing the value of porosity, the effects of asymmetric material response decrease.

## Conclusion

This article deals with study of the effects of asymmetric material response of dense SMAs on the mechanical properties of porous products. To achieve this goal, a 3D constitutive model considering this behavior was developed based on microplane theory. The model was then used to attribute material behavior of SMAs to corresponding unit cell models. The results of AM were compared with experiment and previous model, and a good correlation was observed. The results obtained by the SMT and SMC were also compared with those obtained by AM. It was realized

that in comparison with the other two models, predictions of the AM are closer to experimental findings. In addition, the effects of asymmetric material response on the hysteresis area of stress–strain curve in tension and compression for several levels of porosity were assessed. It was concluded that by increasing the value of porosity, the difference between the hysteresis area in tension and compression decreased. Finally, the stress–strain response of superelastic BCC and BCC-Z cellular lattice structures was investigated using symmetric model with tensile and compressive material parameters as well as AM. The obtained results illustrates that the asymmetric material response can affect the stress–strain response of lattice structures. In addition, in comparison with the AM, a less stress level is predicted using the SMT and SMC, while the SMC over-predicts the stress level. Also, the effects of asymmetric material response are decreased by decreasing the value of porosity and increasing the portion of axial loading in deformation mechanisms of the lattices.

## Acknowledgements

All the simulations are performed in National High-Performance Computing Center of Isfahan University of Technology. The authors would also like to thank Dr Ashrafzadeh for making it possible to use the facilities of National High-Performance Computing Center.

## Declaration of Conflicting Interests

The author(s) declared no potential conflicts of interest with respect to the research, authorship, and/or publication of this article.

## Funding

The author(s) received no financial support for the research, authorship, and/or publication of this article.

## References

- Altenbach H and Oechsner A (2011) *Cellular and Porous Materials in Structures and Processes*. New York: Springer Science & Business Media.
- Auricchio F and Petrini L (2004) A three-dimensional model describing stress-temperature induced solid phase transformations: solution algorithm and boundary value problems. *International Journal for Numerical Methods in Engineering* 61: 807–836.
- Auricchio F and Taylor RL (1997) Shape-memory alloys: modelling and numerical simulations of the finite-strain superelastic behavior. *Computer Methods in Applied Mechanics and Engineering* 143: 175–194.
- Bechle NJ and Kyriakides S (2014) Localization in NiTi tubes under bending. *International Journal of Solids and Structures* 51: 967–980.
- Böhm HJ (2004) *A Short Introduction to Continuum Micromechanics*. New York: Springer.
- Bouvet C, Calloch S and Lexcellent C (2004) A phenomenological model for pseudoelasticity of shape memory alloys under multiaxial proportional and nonproportional loadings. *European Journal of Mechanics: A/Solids* 23: 37–61.
- Brocca M, Brinson L and Bažant Z (2002) Three-dimensional constitutive model for shape memory alloys based on microplane model. *Journal of the Mechanics and Physics of Solids* 50: 1051–1077.
- Carol I and Bazant ZP (1997) Damage and plasticity in microplane theory. *International Journal of Solids and Structures* 34: 3807–3835.
- DeGiorgi VG and Qidwai MA (2002) A computational mesoscale evaluation of material characteristics of porous shape memory alloys. *Smart Materials and Structures* 11: 435.
- Entchev PB and Lagoudas DC (2002) Modeling porous shape memory alloys using micromechanical averaging techniques. *Mechanics of Materials* 34: 1–24.
- Entchev PB and Lagoudas DC (2004) Modeling of transformation-induced plasticity and its effect on the behavior of porous shape memory alloys. Part II: porous SMA response. *Mechanics of Materials* 36: 893–913.
- Freed Y, Aboudi J and Gilat R (2008) Investigation of shape memory alloy honeycombs by means of a micromechanical analysis. *Modelling and Simulation in Materials Science and Engineering* 16: 055002.
- Gall K, Sehitoglu H, Chumlyakov YI, et al. (1999) Tension–compression asymmetry of the stress–strain response in aged single crystal and polycrystalline NiTi. *Acta Materialia* 47: 1203–1217.
- Hassan MR, Scarpa F and Mohamed NA (2009) In-plane tensile behavior of shape memory alloy honeycombs with positive and negative Poisson's ratio. *Journal of Intelligent Material Systems and Structures* 20: 897–905.
- Kadkhodaei M, Salimi M, Rajapakse RKND, et al. (2007a) Microplane modelling of shape memory alloys. *Physica Scripta T129*: 329–334.
- Kadkhodaei M, Salimi M, Rajapakse RKND, et al. (2007b) Modeling of shape memory alloys based on microplane theory. *Journal of Intelligent Material Systems and Structures* 19: 541–550.
- Karamooz RM and Kadkhodaei M (2013) Finite element modeling of the elastic modulus of Ti6Al4V scaffold fabricated by SLM. In: *Poromechanics V5: proceedings of the fifth Biot conference on poromechanics*, Vienna, Austria, 10–12 July, pp. 1021–1028.
- Karamooz Ravari M and Kadkhodaei M (2015) A computationally efficient modeling approach for predicting mechanical behavior of cellular lattice structures. *Journal of Materials Engineering and Performance* 24: 245–252.
- Karamooz Ravari M, Kadkhodaei M, Badrossamay M, et al. (2014) Numerical investigation on mechanical properties of cellular lattice structures fabricated by fused deposition modeling. *International Journal of Mechanical Sciences* 88: 154–161.
- Lagoudas DC and Entchev PB (2004) Modeling of transformation-induced plasticity and its effect on the behavior of porous shape memory alloys. Part I: constitutive model for fully dense SMAs. *Mechanics of Materials* 36: 865–892.
- Lagoudas DC, Entchev PB, Popov P, et al. (2006) Shape memory alloys. Part II: modeling of polycrystals. *Mechanics of Materials* 38: 430–462.
- Lexcellent C, Boubakar M, Bouvet C, et al. (2006) About modelling the shape memory alloy behaviour based on the phase transformation surface identification under proportional loading and anisothermal conditions. *International Journal of Solids and Structures* 43: 613–626.
- Li S (2008) Boundary conditions for unit cells from periodic microstructures and their implications. *Composites Science and Technology* 68: 1962–1974.
- Liu B, Dui G and Zhu Y (2012) On phase transformation behavior of porous shape memory alloys. *Journal of Mechanical Behavior Biomedical Materials* 5: 9–15.
- Liu B, Dui G, Xie B, et al. (2014) A constitutive model of porous SMAs considering tensile-compressive asymmetry behaviors. *Journal of Mechanical Behavior Biomedical Materials* 32: 185–191.
- Lublinter J and Auricchio F (1996) Generalized plasticity and shape memory alloys. *International Journal of Solids and Structures* 33: 991–1003.
- Maitrejean G, Terriault P and Brailovski V (2013a) Density dependence of the macroscale superelastic behavior of porous shape memory alloys: a two-dimensional approach. *Smart Materials Research* 2013: 1–13.
- Maitrejean G, Terriault P and Brailovski V (2013b) Density dependence of the superelastic behavior of porous shape memory alloys: representative volume element and scaling relation approaches. *Computational Materials Science* 77: 93–101.
- Mehrabi R and Kadkhodaei M (2013) 3D phenomenological constitutive modeling of shape memory alloys based on microplane theory. *Smart Materials and Structures* 22: 025017.

- Mehrabi R, Andani M, Kadkhodaei M, et al. (2015) Experimental study of NiTi thin-walled tubes under uniaxial tension, torsion, proportional and non-proportional loadings. *Experimental Mechanics* 6: 1151–1164.
- Mehrabi R, Andani MT, Elahinia M, et al. (2014a) Anisotropic behavior of superelastic NiTi shape memory alloys; an experimental investigation and constitutive modeling. *Mechanics of Materials* 77: 110–124.
- Mehrabi R, Kadkhodaei M and Elahinia M (2014b) Constitutive modeling of tension-torsion coupling and tension-compression asymmetry in NiTi shape memory alloys. *Smart Materials and Structures* 23: 075021.
- Mehrabi R, Kadkhodaei M and Elahinia M (2014c) A thermodynamically-consistent microplane model for shape memory alloys. *International Journal of Solids and Structures* 51: 2666–2675.
- Mehrabi R, Kadkhodaei M, Andani MT, et al. (2014d) Microplane modeling of shape memory alloy tubes under tension, torsion, and proportional tension-torsion loading. *Journal of Intelligent Material Systems and Structures* 26: 144–155.
- Michailidis PA, Triantafyllidis N, Shaw JA, et al. (2009) Superelasticity and stability of a shape memory alloy hexagonal honeycomb under in-plane compression. *International Journal of Solids and Structures* 46: 2724–2738.
- Nemat-Nasser S, Su Y, Guo W-G, et al. (2005) Experimental characterization and micromechanical modeling of superelastic response of a porous NiTi shape-memory alloy. *Journal of the Mechanics and Physics of Solids* 53: 2320–2346.
- Olsen JS and Zhang ZL (2012) Effect of spherical micro-voids in shape memory alloys subjected to uniaxial loading. *International Journal of Solids and Structures* 49: 1947–1960.
- Paiva A, Savi MA, Braga AMB, et al. (2005) A constitutive model for shape memory alloys considering tensile-compressive asymmetry and plasticity. *International Journal of Solids and Structures* 42: 3439–3457.
- Panico M and Brinson LC (2008) Computational modeling of porous shape memory alloys. *International Journal of Solids and Structures* 45: 5613–5626.
- Poorasadion S, Arghavani J, Naghdabadi R, et al. (2013). An improvement on the Brinson model for shape memory alloys with application to two-dimensional beam element. *Journal of Intelligent Material Systems and Structures*. 25: 1905–1920.
- Qidwai MA and Lagoudas DC (2000) On thermomechanics and transformation surfaces of polycrystalline NiTi shape memory alloy material. *International Journal of Plasticity* 16: 1309–1343.
- Qidwai MA, Entchev PB, Lagoudas DC, et al. (2001) Modeling of the thermomechanical behavior of porous shape memory alloys. *International Journal of Solids and Structures* 38: 8653–8671.
- Rahmanian R, Moghaddam NS, Haberland C, et al. (2014) Load bearing and stiffness tailored NiTi implants produced by additive manufacturing: a simulation study. In: *Proceedings of the SPIE 9058, behavior and mechanics of multifunctional materials and composites*, 905814, (March 20, 2014). DOI: 10.1117/12.2048948.
- Reedlunn B, Churchill CB, Nelson EE, et al. (2014) Tension, compression, and bending of superelastic shape memory alloy tubes. *Journal of the Mechanics and Physics of Solids* 63: 506–537.
- Saint-Sulpice L, Chirani SA and Calloch S (2009) A 3D super-elastic model for shape memory alloys taking into account progressive strain under cyclic loadings. *Mechanics of Materials* 41: 12–26.
- Sameallah S, Kadkhodaei M, Legrand V, et al. (2014) Direct numerical determination of stabilized dissipated energy of shape memory alloys under cyclic tensile loadings. *Journal of Intelligent Material Systems and Structures*. Epub ahead of print. DOI: 10.1177/1045389x14549869.
- Sayed TE, Gürses E and Siddiq A (2012) A phenomenological two-phase constitutive model for porous shape memory alloys. *Computational Materials Science* 60: 44–52.
- Sedlak P, Frost M, Benešová B, et al. (2012) Thermomechanical model for NiTi-based shape memory alloys including R-phase and material anisotropy under multi-axial loadings. *International Journal of Plasticity* 39: 132–151.
- Shariat BS, Liu Y and Rio G (2013) Numerical modelling of pseudoelastic behaviour of NiTi porous plates. *Journal of Intelligent Material Systems and Structures* 25: 1445–1455.
- Thamburaja P and Anand L (2001) Polycrystalline shape-memory materials: effect of crystallographic texture. *Journal of the Mechanics and Physics of Solids* 49: 709–737.
- Toi Y and Choi D (2008) Constitutive modeling of porous shape memory alloys considering strain rate effect. *Journal of Computational Science and Technology* 2: 511–522.
- Yu C, Kang G, Kan Q, et al. (2013) A micromechanical constitutive model based on crystal plasticity for thermomechanical cyclic deformation of NiTi shape memory alloys. *International Journal of Plasticity* 44: 161–191.
- Zhao Y and Taya M (2007) Analytical modeling for stress-strain curve of a porous NiTi. *Journal of Applied Mechanics* 74: 291–297.
- Zhao Y, Taya M, Kang Y, et al. (2005) Compression behavior of porous NiTi shape memory alloy. *Acta Materialia* 53: 337–343.
- Zhu P, Stebner AP and Brinson LC (2013) A numerical study of the coupling of elastic and transformation fields in pore arrays in shape memory alloy plates to advance porous structure design and optimization. *Smart Materials and Structures* 22: 094009.
- Zhu P, Stebner AP and Brinson LC (2014) Plastic and transformation interactions of pores in shape memory alloy plates. *Smart Materials and Structures* 23: 104008.
- Zhu Y and Dui G (2010) A macro-constitutive model of polycrystalline NiTi SMAs including tensile-compressive asymmetry and torsion pseudoelastic behaviors. *International Journal of Engineering Science* 48: 2099–2106.
- Zhu Y and Dui G (2011) A model considering hydrostatic stress of porous NiTi shape memory alloy. *Acta Mechanica Sinica* 24: 289–298.

## Appendix I

### Notation

$A_f$	austenite finish temperature	$u$	translational displacement in the $x$ direction
$A_s$	austenite start temperature	$v$	translational displacement in the $y$ direction
$A_{hist}^C$	hysteresis area of stress–strain curve in compression	$w$	translational displacement in the $z$ direction
$A_{hist}^T$	hysteresis area of stress–strain curve in tension	$\beta$	parameter to determine the value of asymmetry
$C_{Af}$	slope of austenite finish in stress–temperature phase diagram	$\delta$	penetration value for porous SMA unit cell model
$C_{As}$	slope of austenite start in stress–temperature phase diagram	$\Delta$	compressive displacement to a unit cell
$C_M$	slope of martensite band in stress–temperature phase diagram	$\varepsilon_D$	total deviatoric strain
$D$	struts' diameter of BCC and BCC-Z lattice structures	$\varepsilon_{ij}$	macroscopic strain tensor
$E$	macroscopic elastic modulus	$\varepsilon_L^+$	maximum recoverable strains in uniaxial tension
$E_A$	austenite elastic modulus	$\varepsilon_L^-$	maximum recoverable strains in uniaxial compression
$E_M^+$	stress-induced tensile elastic modulus of martensite	$\varepsilon_T$	total shear strain
$E_M^-$	stress-induced compressive elastic modulus of martensite	$\varepsilon_V$	total volumetric strain
$E_M^T$	temperature-induced elastic modulus of martensite	$\nu$	Poisson's ratio
$J_2$	second invariant of deviatoric stress tensor	$\xi_T$	temperature-induced martensite volume fraction
$J_3$	third invariant of deviatoric stress tensor	$\xi_s^+$	volume fraction of stress-induced tensile martensite
$L$	unit cell length	$\xi_s^-$	volume fraction of stress-induced compressive martensite
$M_f$	martensite finish temperature	$\sigma_D$	deviatoric part of $\sigma_N$
$M_s$	martensite start temperature	$\sigma_{ij}$	macroscopic stress tensor
$n_i$	components of the unit normal vector, $\mathbf{n}$ , to a microplane	$\sigma_N$	normal stress on a microplane
$R$	radius of spherical pores in unit cell model	$\sigma_T$	shear stress on a microplane
$t_i$	traction vector on a microplane	$\sigma_{Ti}$	components of shear stress vector on a microplane
$\hat{t}_i$	unit vector parallel to resultant shear stress on a microplane	$\sigma_V$	volumetric part of $\sigma_N$
		$\sigma_f^{cr}$	critical stress for finish of detwinning
		$\sigma_s^{cr}$	critical stress for start of detwinning
		$\hat{\sigma}$	modified equivalent stress
		$\Omega$	surface of a unit hemisphere